Hindawi
Geofluids
Volume 2024, Article ID 8816030, 16 pages
https://doi.org/10.1155/2024/8816030

*Research Article*

# Optimization of Support and Relief Parameters for Deep-Buried Metal Mine Roadways

**MingWei Jiang,[1,2,3] YuYun Fan,[4] WeiWei Su,[1,2,3] Jincheng Wang,[1] Ming Lan,[4,5] and Qibin Lin[5]**

[1]*China Coal Research Institute Fushun Branch, Shenfu Demonstration Zone, Fushun 113122, China*
[2]*State Key Laboratory of Coal Mine Safety Technology, China Coal Technology & Engineering Group Shenyang Research Institute, Shenfu Demonstration Zone, Shenyang 113122, China*
[3]*College of Emergency Management and Safety Engineering, China University of Mining and Technology (Beijing), Beijing 100083, China*
[4]*Deep Mining Laboratory of Shandong Gold Group Co., Ltd, Yantai 264000, China*
[5]*School of Resource Environment and Safety Engineering, University of South China, Hengyang 421001, China*

Correspondence should be addressed to Qibin Lin; qblin@usc.edu.cn

Received 31 October 2023; Revised 16 April 2024; Accepted 23 April 2024; Published 20 May 2024

Academic Editor: Wensong Wang



The management of rock mass deformation in high-stress roadways is a pivotal aspect of deep geotechnical engineering. Given the fruitful outcomes of research in rock mechanics regarding traditional confining pressure control methods, scholars have increasingly turned their attention to exploring pressure-relieving techniques, including borehole pressure relief and blasting pressure relief. However, there is limited research on pressure relief methods for deep-buried hard rock tunnels. This article commences with an overview of pressure relief in the roadway and conducts a detailed study on the parameters and methods of pressure relief in the roadway. To address safety and mining efficiency challenges, such as severe deformation leading to support failures, this study conducted a parameter analysis using the Sanshandao Gold Mine as a case study. Based on existing support methods, a strategy for arranging pressure relief roadways at varying distances from the main roadway is proposed, significantly enhancing the stress environment there. Numerical simulation software was employed to model two scenarios: (1) excavating the pressure relief roadway, main roadway, and maintenance roadway simultaneously and (2) first excavating the pressure relief roadway, followed by the main roadway and the maintenance roadway simultaneously. Simulation results indicated that the first pressure relief approach outperforms the second. The optimal position for both pressure relief roadways is 15 m from the main roadway, resulting in maximum deformation of the main roadway within 100 mm. These findings align with on-site stress monitoring data and satisfy safety production criteria. The research offers a theoretical foundation for similar pressure relief techniques in deeply buried, high-stress roadways.

## 1. Introduction

Since long-term and continuous large-scale exploitation has increasingly exhausted shallow metal mineral resources, the exploitation continues continuously deeper into the Earth [1–4]. At present, many metal mines worldwide have successively engaged in deep mining with some extending over 1000 meters underground. Thus, the influence of in situ stress on the stability and failure of the surrounding rock mass becomes more obvious, and the selection of appropriate support parameters [5, 6] and implementing effective ground pressure control techniques under high-stress conditions has become more vital. The excavation process significantly alters the stress state of rock mass, which affects the stability and performance of rock structures. To address the ground pressure issue, many domestic and international scholars have compiled comprehensive research mine pressure control laws and methods, leading to significant

achievements [7–10]. Pressure relief technology is an indirect ground pressure control that creates a weakened zone in the deep portion of the surrounding rock through techniques such as drilling, road opening, and blasting. This provides a designated space for the expansion and deformation of the surrounding rock, enabling the redistribution of concentrated stress to the deeper layers of the rock mass [11–13]. In recent decades, major foreign countries such as South Africa, Poland, Germany, Canada, and the United States have made significant advances in ground pressure control, particularly the drilling pressure relief method developed in Germany, which is widely recognized internationally [14–17]. In China, the typically used pressure relief techniques locally and abroad include hydraulic pressure relief, drilling pressure relief excavation of pressure relief grooves [18, 19], pressure relief tunnels [20], and blasting pressure relief [21, 22]. The advantages and disadvantages of various pressure relief technologies are thoroughly evaluated based on factors such as the distribution pattern of in situ stress, the mechanical response characteristics of the rock mass, and the development of structural planes. Consequently, the most suitable pressure relief technology and corresponding parameters are determined [23, 24].

Lei et al. [25] maintained that for shallow-buried tunnels with minimal clear distance, the deep-buried side's surrounding rock mass requires reinforcement independent of the tunnel's surrounding rock. Furthermore, the consolidation scope must extend beyond the tunnel's midline (in the slope's top direction) by 4 spans of a single tunnel's excavation. Mohtadinia et al. [26] utilized numerical simulation techniques to investigate the stress characteristics of lining support, providing a foundation for its application. Xu et al. [27] introduced a pressure relief approach that entails creating relief slots in the roof and floor of a circular opening, considering the nonuniform stress distribution around such an opening under anisotropic far-field stress. Chen and Liu [28] conducted research on large-diameter partition pressure relief technology for deep mining tunnels; they comprehensively analyzed the blast hole's diameter, depth, and inclination angle, ultimately determining optimal pressure relief parameters. Luo et al. [29] studied on blasting pressure relief in high-stress areas emphasized the significant impact of nonpenetrating fractures resulting from blasting on tunnel stability, and safer blasting practices in deeper locations were recommended. Geng et al. [30] through creep test and long-term on-site observation researched the secondary support time and support parameter selection for deep tunnel secondary support to provide reference for deep tunnel secondary support. Currently, research on pressure relief is primarily focused on coal science and technology, while the research in this area for metal mine remains limited.

Addressing the aforementioned issues, our study is aimed at investigating effective unloading methods and supporting strategies during the unloading process of high-stress tunnels in deep metal mines. To achieve this, we utilized a triaxial dynamic-static loading system to conduct triaxial static load tests on coal and rock samples. This allowed us to examine the impact of varying triaxial stress conditions on rock failure and the differences in failure modes. Furthermore, on-site testing of rock mass quality parameters in deep-buried tunnels enabled us to analyze the factors influencing rock mass quality. We also explored the relationship between the rock mass's loosening zone and support components through anchor rod pull-out tests and loosening zone tests. These tests provide a fundamental basis for tunnel support design. By integrating theoretical analysis, numerical calculations, on-site experiments, and other methods, we determined the optimal unloading distance and support parameters. Long-term on-site monitoring has demonstrated that the pressure relief roadway significantly mitigates pressure on high-stress roadway props. This finding offers valuable insights for the design of surrounding rock support for high-stress roadway structures facing similar disturbances.

## 2. Project Overview

In this study, Sanshandao Gold Mine located in Shandong Province, China, serves as the primary engineering case, with a mining depth exceeding 1000 meters. The in situ stress measurement results indicate that the stress magnitude in this region is approximately 50 MPa. Under influence of high in situ stress, safe and effective mining at depth is facing a series of engineering challenges, including the prediction and prevention of rock burst, rock support techniques, redistributed stresses, and large deformation. The permanent main roadway of -1140 m level is a typical case of such engineering conditions. The stress along the section of roadway is highly concentrated owing to the absence of neighboring projects. Currently, the roadway has apparent fragmentation signs of fragmentation and severe deformation due to the prominent significant ground pressure, as shown in Figure 1. It has been observed that the current support parameters are inadequate to the high-stress environment; the safety of the roadway will inevitably be endangered. Therefore, it is proposed to optimize support parameters and take a suitable pressure relief technology to improve the surrounding rock stress environment through systematic research.

## 3. Determination of Pressure Relief Plan

*3.1. Loose Ring Test.* The ground-based radar was employed to identify the roadway's loose ring and inform the selection of bolt length for main roadway support. The radar detection chart reveals that the anchor rod and anchor net have some impact on the geological radar signal. As shown in Figure 2(a), the reflection of electromagnetic waves in the red circle is disorder, which is speculated that there could be serious damage here. In the vertical axis section of the radar detection image, clear wave reflection boundaries can be observed, indicating apparent fractures at 2.5 m and 3.5 m. The cross-sectional radar grayscale image (Figure 2(b)) clearly reveals that there is an obvious reflection interface at approximately 2.5 m. In other words, the range of the loose ring is 2.5 m.

Figure 1: High-stress-induced instability of surrounding rock.

*3.2. Bolt Drawing Test.* To investigate the support effect of bolt with different lengths within the range of loose ring, as the length of bolt in the current support scheme is 2.2 m, a series of bolt drawing tests were conducted. Measuring the length of bolt at 2 m, 2.5 m, 3 m, and 3.5 m, they were installed in the study area. Figure 3 presents the bolt drawing load test system. Subsequently, the drawing test was executed. Table 1 displays the results, indicating that when the length of bolt is 2 m, 2.5 m, 3 m, and 3.5 m, the corresponding average maximum drawing load of the bolt is 21 kN, 50 kN, 252 kN, and 269 kN, respectively. The test curves are shown in Figure 4.

The test results indicate a significant improvement in bolting force once the bolt length exceeds the range of the loose ring. This enhances the stability of the bolt-roadway combination, enabling it to produce the desired support effect. Based on the results of the loose ring test and bolt drawing test, it is recommended that the short cable length should exceed 3 meters.

The current bolt support length for this roadway measures 2.2 meters, with the effective range of the support being confined within the loose circle. Consequently, the bolt support is not achieving the desired effect. In response to this situation, a combined support method utilizing anchor rod and anchor cable and beam is proposed. Building upon the original support, a row of beams onto the roadway roof was introduced, accompanied by two anchor cables positioned at both ends of each beam. The anchor cables measure 8 meters in length, the beams are 2 meters long, and the distance between each support row is set at 1 meter. Figure 5 provides a visual representation of this support method. Based on the current support, two pressure relief schemes are proposed. The initial step under this scheme involves excavating the pressure relief roadway, followed by subsequent excavation of the main roadway and the TBM start roadway. By simulating the stress and deformation of the main roadway under various scenarios where the distance between the pressure relief roadway and the main roadway varies from 5 meters to 10 meters, 15 meters, and ultimately 20 meters, our aim is to identify the optimal pressure relief environment.

*3.3. Mapping of Geological Discontinuity.* During underground mining, the primary factor impacting rock stability is the quality level of the rock mass. The quality level of the rock mass is intimately linked to the parameters such as internal joints, fractures, and dip angles of those fractures. Furthermore, the quality level of the rock mass also impacts the selection of support parameters. The shape, mechanical properties, and spatial combination conditions of soft structural plane significantly impact rock mass stability. In this study, a geological discontinuity mapping and analysis system (Sirovision) was utilized used to investigate the structural plane of the roadway. There were six separate measurement areas, with a total length spanning 43 meters. Figure 6 displays both left and right photographs, along with the derived three-dimensional rock mass map from this image. As shown in Figure 7, a three-dimensional model of the rock mass in test area #1 is developed by integrating various photographs.

In this section, we focus solely on test area #1. However, the same analytical approach can be applied to other test areas. Using the system's software, the integrated images and the red plane projection method to generate pole diagrams were processed, Schmidt isodensity diagram, and rose diagram for the joints in each test area. Figure 8 displays the pole diagram, Schmidt isodensity diagram, and rose diagram of the exposed joints on the surface of the rock mass within the confines of test area #1. Based on the data clustering results, the following parameters for test area #1, 35 joints, a joint spacing of 0.56 m, a trace length of 1.59 m, a dip angle of 42.3°, and an additional dip angle of 85.78°, were obtained. These parameters provide valuable insights into the structural characteristics and spatial distribution of joints within the test area.

*3.4. Laboratory Test*

*3.4.1. Rock Material and Test Preparation.* The granite extracted from the -1140 m level of Sanshandao Gold Mine needs to undergo processing to create a cylindrical piece with a diameter of $\Phi$50 mm and length of 100 mm, as shown in Figure 9(a). This matches the recommended sample size established by the International Society for Rock Mechanics (ISRM). Through preliminary tests, the uniaxial compressive strength and tensile strength of the granite have been determined as 81.85 MPa and 11.71 MPa, respectively.

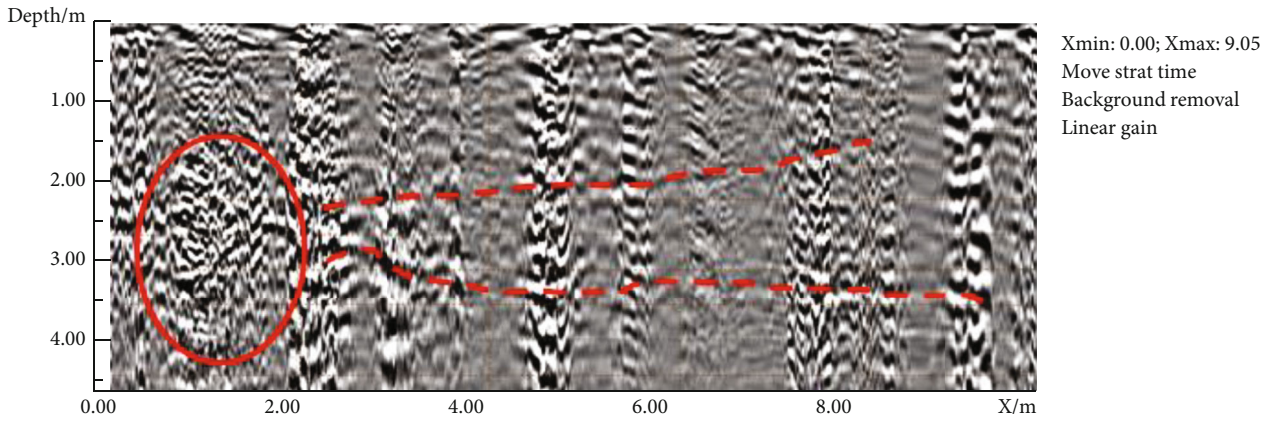


(a) Roadway roof axis radar detection image

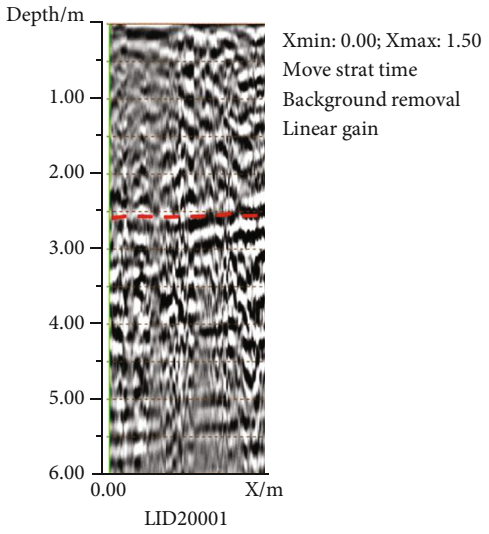


(b) Vertical axis section radar detection image

Figure 2: Geological radar detection map.

Figure 3: Conventional triaxial rock mechanics testing machine.

Table 1: Average drawing load of bolts at different lengths.

| Bolt length (m) | 2 | 2.5 | 3 | 3.5 |
|---|---|---|---|---|
| Drawing load (kN) | 21 | 50 | 252 | 269 |

Figure 9(b) displays the ZTR-276 electrohydraulic servo rock triaxial test system, which is utilized in triaxial compression tests conducted in the Deep Mining Laboratory of Shandong Gold Group Co., Ltd. The granite specimens are shown in Figure 9(c).

*3.4.2. Test Scheme.* A conventional triaxial compression test for two primary reasons was conducted. Firstly, it is aimed

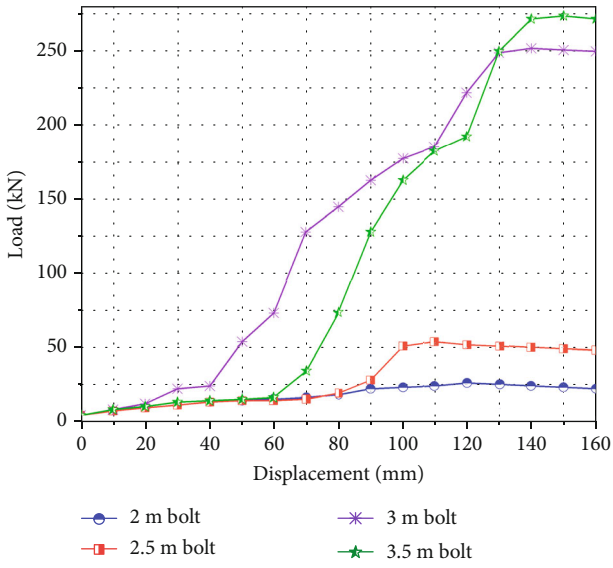


Figure 4: Bolt drawing test curves of different buried depths.

at analyzing the mechanical properties of rocks under loading conditions, with the aim of utilizing the test results in subsequent numerical simulation experiments. Secondly, it provides data support for subsequent rock quality classification.

The triaxial compression tests are executed with a constant loading rate of 500 N/s under progressively increasing stress. According to the in situ stress measurements, the confining pressures are set at 10 MPa, 20 MPa, 30 MPa, and 40 MPa, respectively.

*3.4.3. Test Results and Discussion.* Figure 10 displays the complete stress-strain curve at an initial confining pressure of 30 MPa. As can be observed from the figure, the stress increased almost linearly with strain until it reaches its maximum. Postpeak curves exhibit distinct elastic-brittle characteristics and a stress drop phenomenon, indicating a brittle nature. Following the failure of the rock sample, the residual strength remains at a low value.

Table 2 displays the physical and mechanical parameters of rock that were calculated using experimental data.

## 4. Rock Mass Quality Classification and Optimization of Support Parameters

*4.1. Rock Mass Quality Classification.* The basic rock mechanics parameters in this region were determined through indoor rock mechanics experiments and other technical methods. Utilizing the $Q$ rock classification system proposed by Norwegian geologist Barton et al., the roadway rock quality grade was further subclassified. The results of this analysis are summarized in Table 3.

$$Q = \frac{\mathrm{RQD}}{J_n} \cdot \frac{J_r}{J_a} \cdot \frac{J_w}{\mathrm{SRF}}, \quad (1)$$

where RQD is a metric used to assess the quality of rock masses, $J_n$ is the number of joint groups, $J_r$ is the roughness coefficient, $J_a$ is the joint alteration coefficient, $J_w$ is the joint water reduction coefficient, and SRF is the in situ stress reduction coefficient.

The rock masses in the ore bodies and surrounding rocks of the Sanshandao Gold Mine study area, based on the $Q$ system classification, fall within classes IV and V. Notably, certain sections of the E3 survey area are classified as class V, indicating a lower quality. It is imperative to pay close attention to potential rock mass instability during construction, necessitating a robust support network with diverse support methods.

After conducting rock mechanics experiment and field joint fracture surveys, the following parameters were determined: RQD value of 80, $J_n$ value of 9, $J_r$ value of 1.5, $J_a$ value of 1, $J_w$ value of 1, SRF value of 2, and $Q$ grading score of 37.50, indicating a generally grade IV rock mass.

*4.2. Optimization of Support Parameters.* Based on Matthew's diagram, which illustrates the correlation between rock mass stability and the $Q$ value, it is essential to implement reinforced support in this region. Bolt spacing should not exceed 2 meters. However, the current bolt support length in this roadway measures 2.2 meters, and the cable's support range does not encompass the loosening ring, leading to inadequate support. In light of these findings, a combined support approach—consisting of short cable and anchor cable and beam—is proposed to enhance support. As Figure 11 depicts, a row of beams is installed on the roadway roof, with two bolts positioned at both ends of each beam. The anchor cable measures 8 meters in length, the short cables are 3 meters long, and the beams are 2 meters long. The distance between each row of supports is set at 1 meter.

## 5. Parameter Determination and Effect Simulation of Pressure Relief Scheme

*5.1. Arrangement of Pressure Relief Roadway Parameter*

*5.1.1. Viscoelastic Analysis of Failure Mechanism of Surrounding Rock.* In this section, viscoelastic analysis of the deformation law of the surrounding rock in the roadway without support was conducted, utilizing the creep model and rock damage model. The time-dependent stress behavior in the surrounding rock was also delved. It is important to note that even within the same in situ stress field, variations in mechanical effects can be attributed to distinct geological environments. Typically, the evolution of deformation and stress in the surrounding rock of roadways follows a similar pattern. Based on these assumptions, the creep model and Kelvin-Voigt (K-V) model for the roadway were considered:

(1) The surrounding rock is considered a homogeneous and isotropic linear viscoelastic body, possessing consistent physical properties throughout its volume

(2) The surrounding rock exhibits elastic behavior, adhering to the principles outlined by the Burgers viscoelastic model


Figure 5: Numerical model.

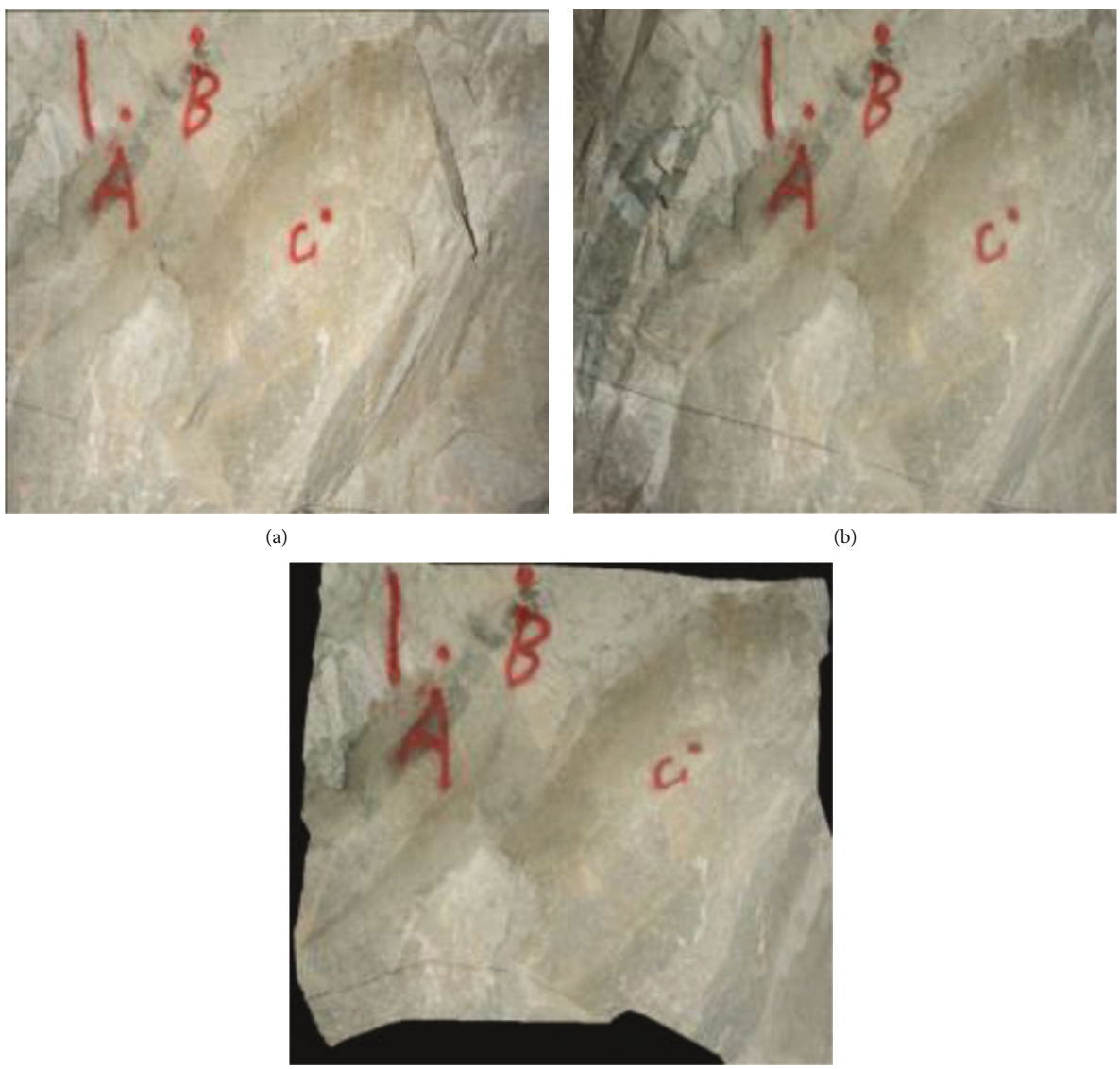


(a) (b)

(c)

Figure 6: On-site photo stitching: (a) on the left; (b) on the right; (c) 3D picture.

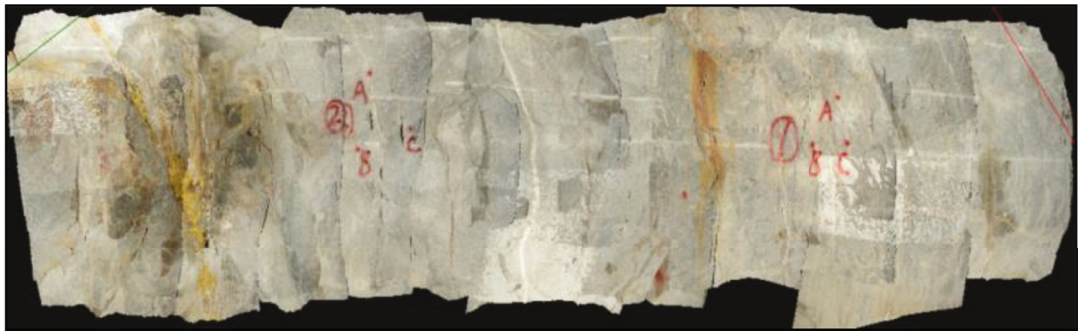

Figure 7: Generation of model of the rock surface.

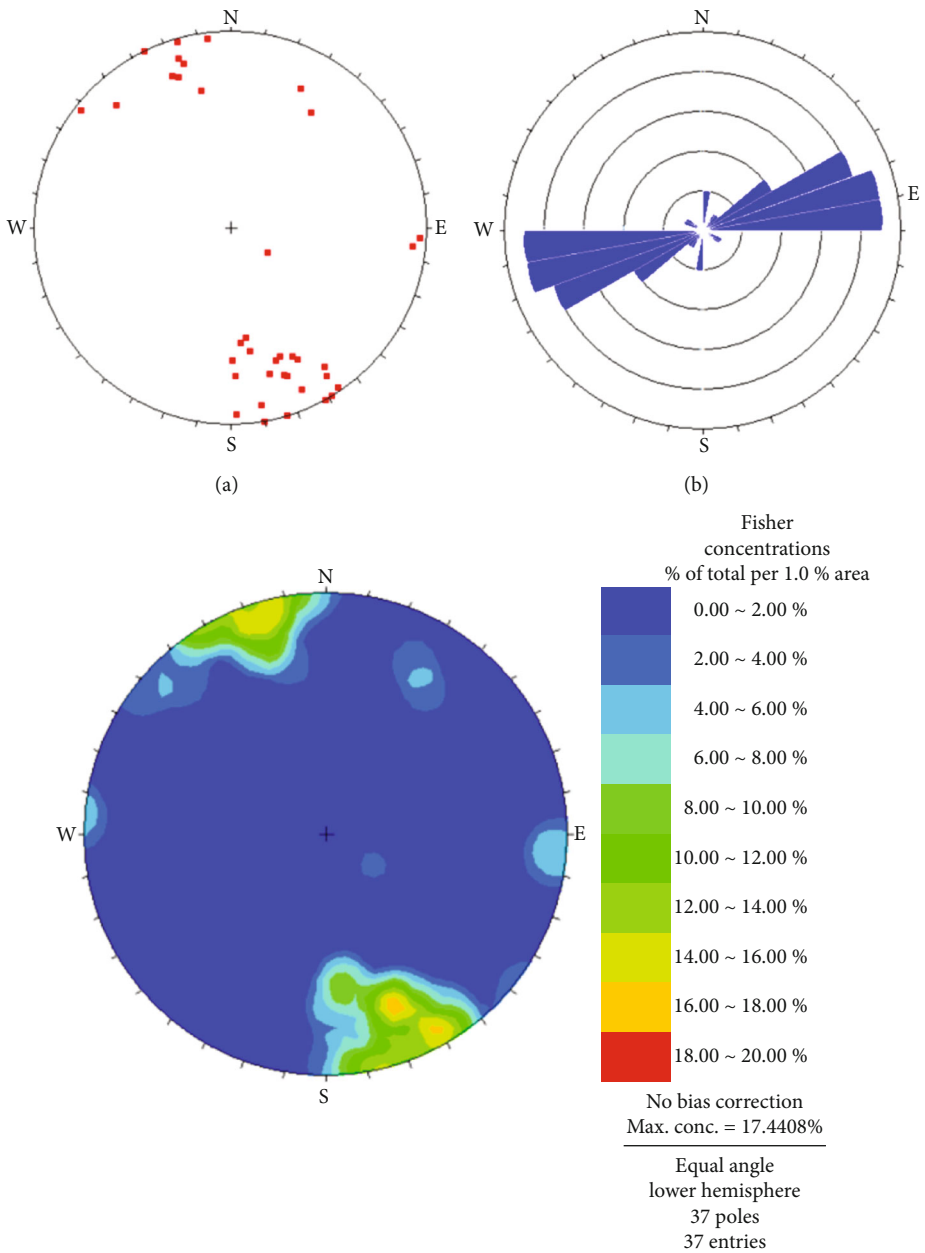


Figure 8: Structural plane occurrence information in test area #1: (a) diagram of the poles; (b) rose picture; (c) Schmidt isodensity diagram.

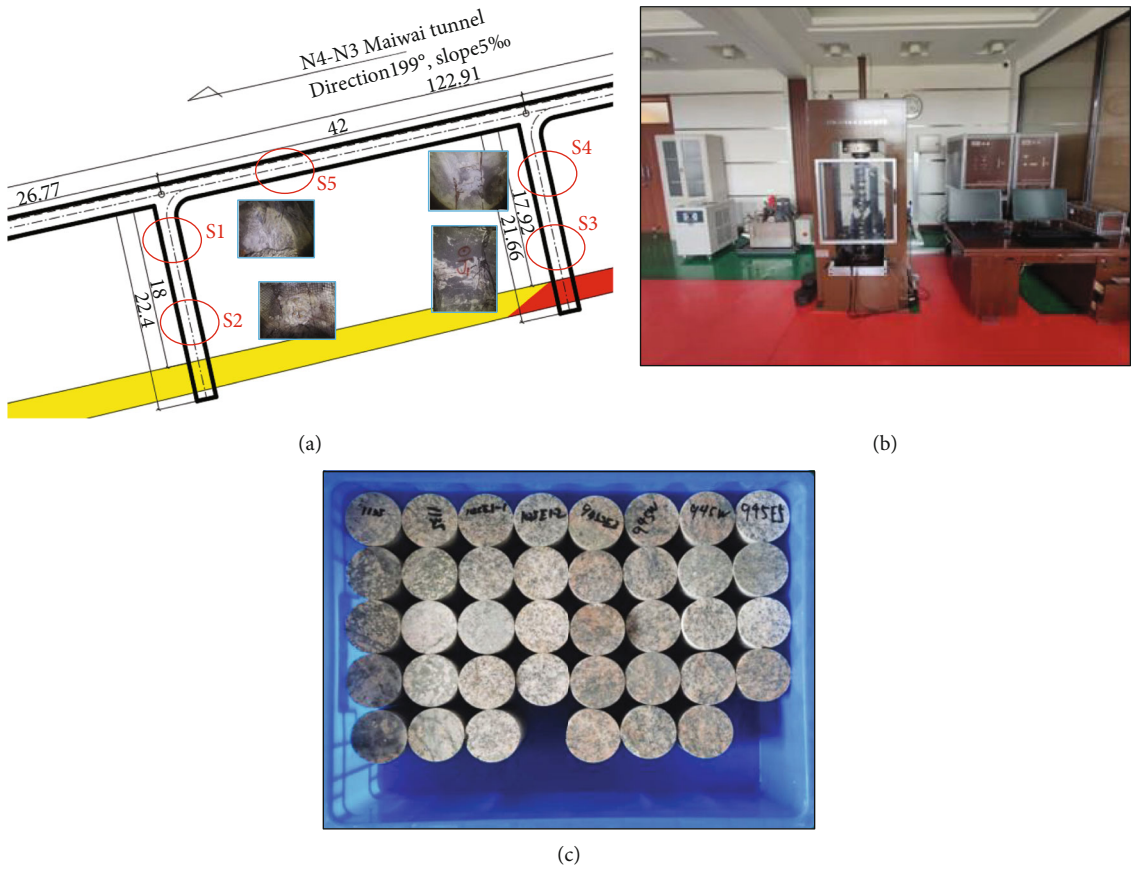


Figure 9: Mechanical test equipment and granite specimens: (a) specimen selection position; (b) ZTR-276 electrohydraulic servo rock triaxial test system; (c) granite specimen.

(3) For simplicity, assuming that the roadway is embedded in an infinite viscoelastic medium, eliminating boundary effects

(4) Assuming that the stress state of the original rock is isotropic and isobaric, with a constant stress level of $q$

(5) Disregarding the self-weight of the rock mass surrounding the roadway, maintaining the assumption of an infinite viscoelastic body for the roadway

(6) To facilitate analysis, neglecting the influence of excavation disturbances on the surrounding rock

In the unsupported condition, the stress in the surrounding rock is as follows:

$$\begin{aligned}
\sigma_r &= \frac{p+\lambda p}{2}\left(1-\frac{a^2}{r^2}\right)+\frac{p-\lambda p}{2}\left(1-\frac{4a^2}{r^2}+\frac{3a^4}{r^4}\right)\cos 2,\\
\sigma_\theta &= \frac{p+\lambda p}{2}\left(1-\frac{a^2}{r^2}\right)+\frac{p-\lambda p}{2}\left(1+\frac{3a^4}{r^4}\right)\cos 2\theta,\\
\tau_{t\theta} &= \frac{p+\lambda p}{2}\left(1+\frac{2a^2}{r^2}+\frac{3a^4}{r^4}\right)\sin\theta.
\end{aligned} \tag{2}$$

When the deformation of the rigid body itself is disregarded, the elastic displacement in the surrounding rock can be determined through the physical equation and the geometric equation as outlined below:

$$\begin{aligned}
u_r = &-\frac{(1-\mu^2)}{2E}P\left[(1+\lambda)\left(r+\frac{a^2}{r}\right)\right.\\
&\left.-(1-\lambda)\left(r+\frac{4a^2}{r}-\frac{a^4}{r^3}\right)\cos 2\theta\right]\\
&+\frac{(1+\mu)}{2E}p\left[(1+\lambda)\left(r-\frac{a^2}{r}\right)\right.\\
&\left.+(1-\lambda)\left(r-\frac{a^4}{r^3}\right)\cos 2\theta\right],
\end{aligned} \tag{3}$$

$$\begin{aligned}
u_\theta = &-\frac{(1-\mu^2)}{2E}P\left[(1-\lambda)\left(r+\frac{2a^2}{r}-\frac{a^4}{r^3}\right)\sin 2\theta\right]\\
&-\frac{(1+\mu)}{2E}p\left[(1-\lambda)\left(r-\frac{2a^2}{r}+\frac{a^4}{r^3}\right)\sin 2\theta\right].
\end{aligned} \tag{4}$$

In formula (3), if $a = 0$, it follows that the elastic displacement in the surrounding rock under the influence of ground stress before the excavation of the roadway is given by

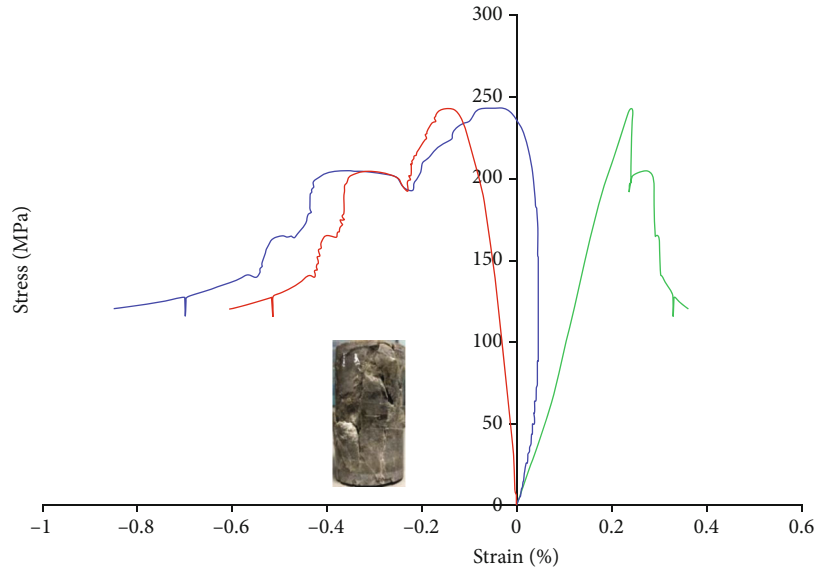


Figure 10: Full stress-strain curve under confining pressure of 30 MPa.

Table 2: Mechanical parameter of granite.

| Confining pressure (MPa) | Peak stress (MPa) | Elastic modulus (GPa) | Poisson's ratio | Cohesion (MPa) | Internal friction angle (°) |
|---|---|---|---|---|---|
| 10 | 162.20 | 44.629 | 0.23 | 12.428 | 47.749 |
| 20 | 216.57 | 47.776 | 0.26 | | |
| 30 | 296.17 | 48.066 | 0.29 | | |
| 40 | 325.51 | 49.637 | 0.32 | | |

Table 3: Grading results.

| Test location | E1 | E2 | E3 |
|---|---|---|---|
| RQD | 29.45 | 33.66 | 20.51 |
| $J_n$ | 2 | 2 | 2 |
| $J_r$ | 1 | 1 | 2 |
| $J_a$ | 4 | 5 | 5 |
| $J_w$ | 1 | 1 | 1 |
| SRF | 2 | 2 | 3 |
| $Q$ | 0.69 | 0.63 | 0.09 |
| Grade | IV | IV | V |

$$u_{r0} = -\frac{(1-\mu^2)}{2E}P[(1+\lambda)r - (1-\lambda)r\cos 2\theta] + \frac{(1+\mu^2)}{2E}p[(1+\lambda)r + (1-\lambda)r\cos 2\theta], \quad (5)$$

$$u_{\theta 0} = -\frac{(1-\mu^2)}{2E}P[(1-\lambda)r\sin 2\theta] + \frac{\mu(1+\mu)}{2E}p[(1-\lambda)r\sin 2\theta]. \quad (6)$$

After solving (4) and (5), the actual displacement after excavation of the roadway can be derived as

$$u_r = -\frac{(1-\mu^2)}{2E}P\left[(1+\lambda)\frac{a^2}{r} - (1-\lambda)\cos 2\theta\right] + \frac{\mu(1+\mu)}{2E}p\left[(1+\lambda)\frac{a^2}{r} + (1-\lambda)\frac{a^4}{r^3}\cos 2\theta\right],$$
$$u_{\theta a} = -\frac{(1-\mu^2)}{2E}P[(1-\lambda)\sin 2\theta] - \frac{\mu(1+\mu)}{2E}p\left[(1-\lambda)\left(\frac{2a^2}{r} + \frac{a^4}{r^3}\right)\sin 2\theta\right]. \quad (7)$$

By utilizing formula (6) with the given parameters ($p = 20$ MPa, =0.3, $E = 3700$ MPa, and $a = 3$ m, 0.5, 0.8, 1.0, and 1.2, respectively), the radial displacement curve of the surrounding rock with respect to the radius can be determined. It is observed that when the lateral pressure coefficient remains constant, the displacement of each point within the surrounding rock diminishes as the distance from the roadway center increases, ultimately approaching zero at infinity. Additionally, as the roadway radius increases, the displacement also increases. Furthermore, for points at the same distance from the roadway center, the displacement decreases as the lateral pressure coefficient rises.

*5.1.2. Selection of Pressure Relief Lane Width.* The size of the pressure relief roadway has a direct impact on the quality of the pressure relief effect, making it imperative to

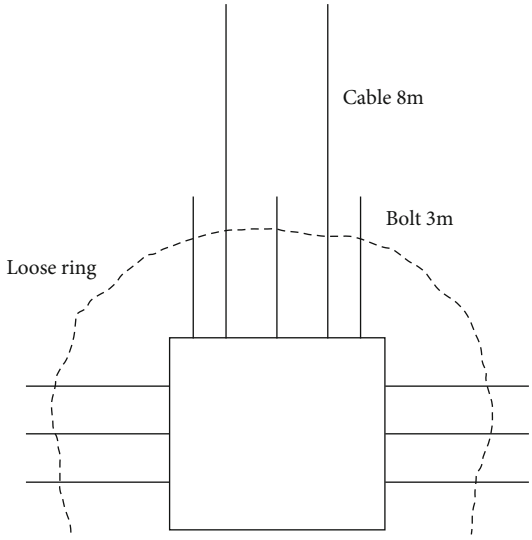


Figure 11: Schematic diagram of support.

scientifically and reasonably select the size of the county government roadway.

$$d = \frac{SW}{2M}, \tag{8}$$

where $S$ is the excavation area of the main roadway ($S = 15.64\,\text{m}^2$); $W$ is the shrinkage rate of the roadway section when there is no pressure relief roadway, generally 50%; and $M$ is the height of the pressure relief roadway, which is determined to be 2 according to the on-site mechanical equipment.

The minimum width of the pressure relief roadway, $d$, is calculated to be 1.955 meters. Hence, for practical purposes, the width is rounded up to 2 meters.

*5.1.3. Selection of Pressure Relief Lane Distance.* Calculation of the total load over the yield distance of the roadway is as follows:

$$P = L_p \gamma H, \tag{9}$$

where $P$ is yield load and $L_p$ is the width of the loading belt $L_p = (0.5b + L_n + d)/2$. The width of the main roadway is taken as 4 m; $\gamma$ is the bulk density of the overlying rock layer, which is $25\,\text{kN/m}^3$; $H$ is the buried depth of the roadway, which is 1000 m.

The upper limit bearing capacity of the yield width is

$$Q = L_n R \left(\frac{L_n}{M}\right) \frac{2}{3}. \tag{10}$$

To determine the yield distance, we consider the ultimate compressive strength on the yield width, $Q$, which is 12 MPa.

The leading support pressure concentration coefficient of the mining face is specified as $k = 3$. By utilizing this coefficient, we calculate the yield distance using the formula $k_P = Q$, obtaining a yield distance of 14.75 meters. For practical considerations, this distance is rounded up to 15 meters.

Table 4: Mechanical parameter of the rock mass.

| Parameter | Density ($\text{kg·m}^{-3}$) | Bulk (GPa) | Shear (GPa) | Friction (°) | Cohesion (MPa) |
|---|---|---|---|---|---|
| Rock mass | 2700 | 11.63 | 5.84 | 29 | 0.5 |

*5.1.4. Determination of Pressure Relief Scheme.* Based on the field tests and theoretical calculations provided, two pressure relief schemes utilizing the combined support method are proposed.

Scheme 1: excavate the pressure relief roadway first, followed by the main roadway. Finally, the start roadway is excavated. Scheme 2: simultaneously excavate the pressure relief roadway, main roadway, and start roadway. To determine the optimal pressure relief environment, we simulate the stress and deformation of the main roadway at various distances between the pressure relief roadway and the main roadway of 5 m, 10 m, 15 m, and 20 m. Subsequently, at the optimal pressure relief distance, two scenarios, excavating the pressure relief roadway first and excavating it simultaneously, are simulated, aiming to optimize the scheme and identify the most effective pressure relief approach.

### 5.2. Numerical Simulation of Pressure Relief

*5.2.1. Establishment of the Numerical Model.* To accurately represent the actual site, the numerical simulation model used in this research is designed to be 100 m long, 20 m wide, and 50 m tall. The Mohr-Coulomb model is employed for this study. The bottom surface of the model is fixed, while stress constraints are applied in the $X$-direction and $Y$-direction. The upper portion is left free. Based on the burial depth and local geological conditions, the vertical stress in this area is set at 27 MPa, and the horizontal stress is the initial in situ stress of 20 MPa. Therefore, a uniform vertical stress of 27 MPa must be applied to the top of the model.

To enhance the accuracy of the simulation, the mesh division within the model is carefully designed. The upper 25 meters of the model is divided into 1-meter units, the middle 10 meters is divided into 0.5-meter units, and the lower 15 meters is divided into 1-meter units. This yields a total of 530960 units and 2386613 nodes in the model. The model diagram is presented in Figure 5. For research purposes, the simulation process simplifies the working face as a horizontal rock formation. Table 4 provides a comprehensive list of the physical parameters used in the model.

*5.2.2. Simulation Process and Analysis.* Based on the previously described support design, we consider the first scenario of excavating the main roadway without a pressure relief system. In this scenario, the maximum displacement of the roadway reaches 260 mm, indicating severe deformation that could pose potential safety risks if mining continues. To address these concerns, we propose the first scheme of excavating a pressure relief roadway with a cross-sectional area of 2 m × 2 m. This scheme is aimed at achieving balance after excavation by initiating the lane,

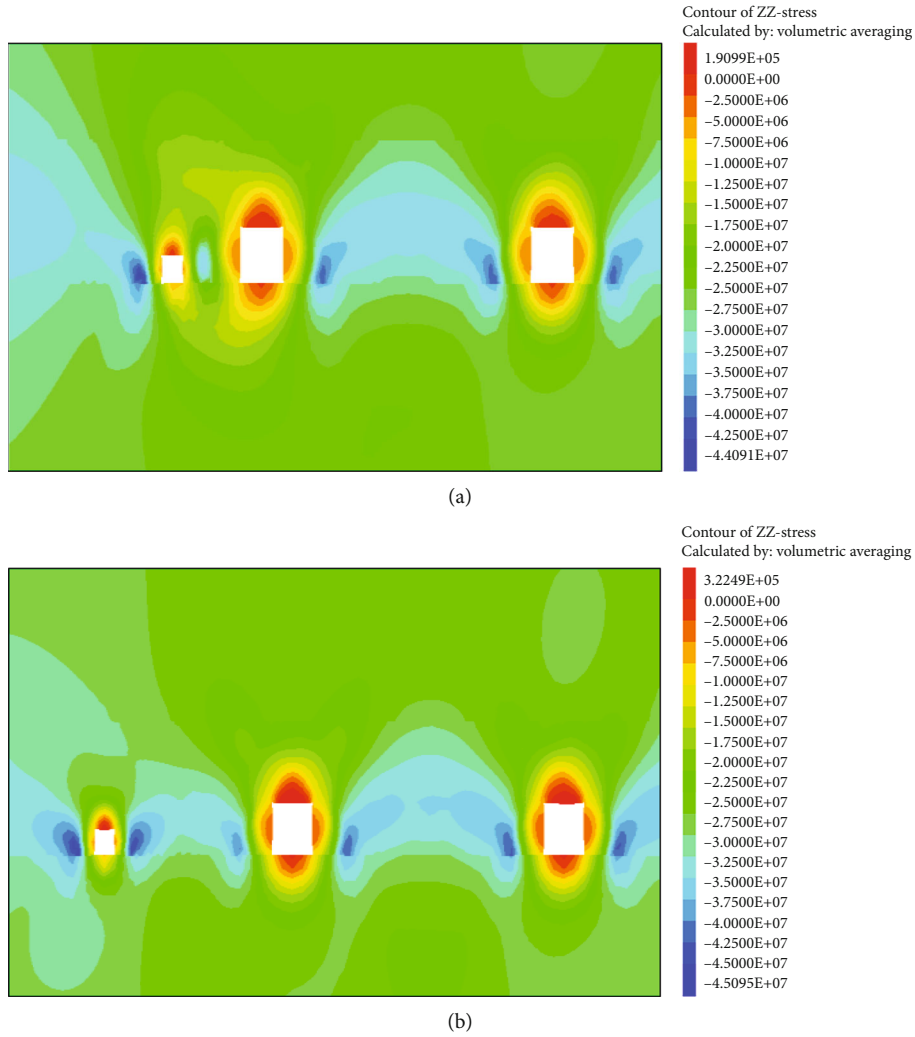


Figure 12: Scheme 1 stress contour: (a) stress nephogram with a spacing of 5 meters; (b) stress nephogram with a spacing of 15 meters.

followed by calculations to balance the load. The width of the two lanes is set at 4.5 m × 4 m, and the support method remains identical. The second scheme involves simultaneously mine three roadways, with the construction progress of the pressure relief roadway always leading the other two main roadways by a minimum of 5 meters. To monitor displacement and stress, monitoring points are placed at 5 m intervals in the main roadway and roof. The displacement and stress changes of the main roadway were observed when the pressure relief roadway is situated 5 meters, 10 meters, 15 meters, and 20 meters away from the main roadway. Drawing from simulation results and previous research, we focus our analysis on the 5 m and 15 m spacings. These spacings are selected as they represent significant changes in displacement and stress patterns that are crucial for understanding the behavior of the system under consideration.

In Figures 12 and 13, we can observe the stress distribution in the first and second schemes. It is evident that when the pressure relief roadway spacing is set at 15 meters in both schemes, the stress around the main roadway is significantly reduced. Moreover, the area of highest stress is shifted towards the sides of the pressure relief roadway. In scheme 1, with a 15-meter spacing, the maximum stress concentration is observed within a radius of approximately 0.2 meters around the pressure relief roadway. Conversely, in scheme 2, which implements a similar 15-meter spacing, the maximum stress range around the pressure relief roadway is approximately 0.8 meters. Based on these findings, it can be inferred that the pressure relief effect of scheme 1 is slightly superior to that of scheme 2.

The maximum displacement changes of the main roadway roof at various positions for both schemes are depicted in Figure 14. The data reveals that the displacement of the main roadway in scheme 1's pressure relief method is noticeably lower than that of scheme 2. The curve's overall shape follows a V-shaped, indicating a decrease in roadway displacement from 5 meters to 15 meters. At a distance of 5 meters, the roadway experiences the greatest displacement, which then tapers off at 15 meters. Beyond this point, the displacement once again begins to increase. This suggests that the optimal pressure relief effect is achieved when the pressure relief roadway is situated 15 meters away from the main roadway. By implementing scheme 1, it is possible to maintain the maximum roadway displacement within a

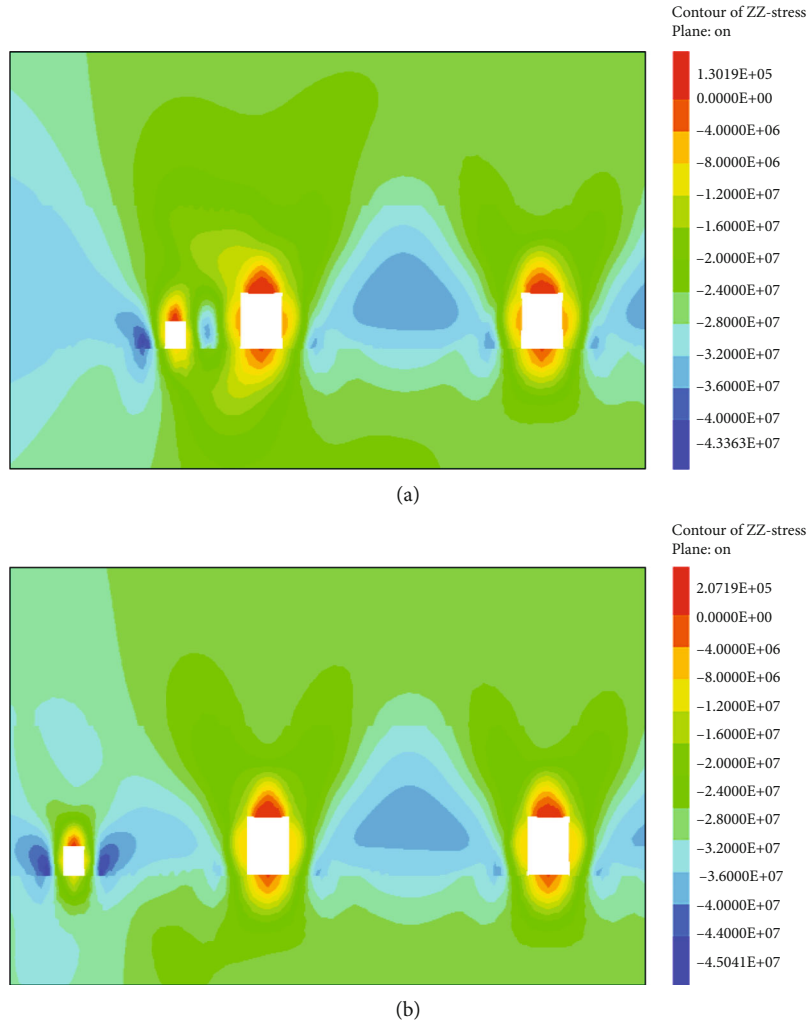


Figure 13: Scheme 2 stress contour: (a) stress nephogram with a spacing of 5 meters; (b) stress nephogram with a spacing of 15 meters.

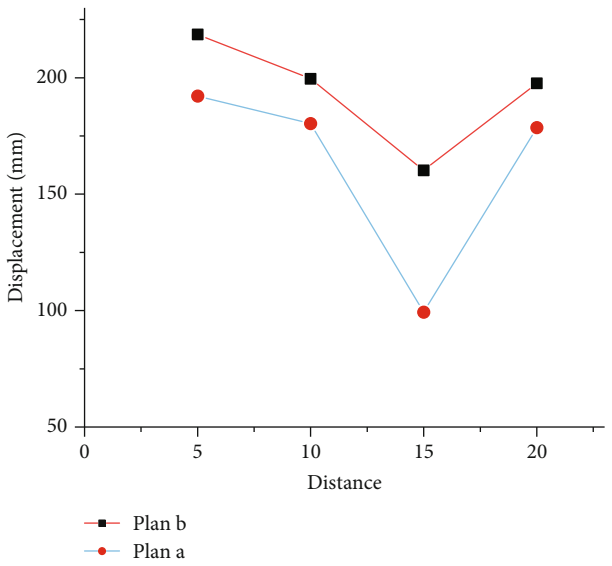


Figure 14: Line chart of main lane position change and displacement.

range of 100 mm, thus ensuring that production safety requirements are met. Furthermore, scheme 1 exhibits a 20% superior deformation rate compared to scheme 2's main roadway, further highlighting its efficacy in meeting these requirements.

## 6. Site Monitoring and Verification

After conducting comprehensive field experimental research and numerical simulations, it has been determined that scheme 1 pressure relief is the most suitable approach to relieve pressure on the main roadway. The distance between the pressure relief roadway and the main roadway has been set at 15 meters, ensuring optimal pressure relief without compromising the stability of the main roadway. As shown in Figure 15(b), the roadway surface exhibits no signs of stress concentration or significant deformation following the pressure relief process. To further evaluate the long-term stability of the roadway, we have implemented a ground pressure monitoring program. This ongoing monitoring will provide precise insights into the behavior of the roadway after construction, enabling us to identify any

(a) (b)

Figure 15: Comparison of roadway stability before and after pressure relief: (a) before roadway pressure relief; (b) after roadway pressure relief.

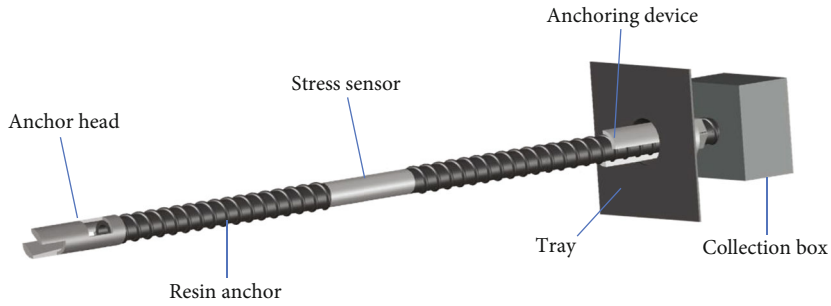


Figure 16: Monitoring system structure diagram.

potential issues or instabilities. The data obtained from this monitoring will inform our decision-making process and guide future improvements to enhance the durability and performance of the roadway.

*6.1. Monitoring System and Monitoring Content.* A ground pressure monitoring system is a crucial component of mine safety management, which assumes the responsibility of preventing and resolving major safety risks and responding promptly to various ground pressure catastrophes. In this study, a new type of deep ground pressure monitoring system for metal mines is used to monitor the stability of roadways, which can simultaneously monitor rock vibration signals and stress signals in real time. The system can achieve wireless data transmission. The component of the ground monitoring system is shown in Figure 16.

This monitoring focuses primarily on the on-site test of scheme 1. A set of system is installed on the roof of the main roadway and the pressure relief roadway to monitor the stress and vibration signals during the excavation process. The monitoring location is shown in Figure 17.

*6.2. Monitoring Results and Analysis.* The red lines in Figure 18 represent the stress changes in the main roadway and pressure relief roadway. As observed, there was no significant stress variations in either roadway prior to monitoring in the preceding week. Beginning on December 14th, the stress in the main roadway decreased rapidly from 44 MPa to 35 MPa and subsequently stabilized. Conversely, the stress in the pressure relief roadway increased rapidly from 36 MPa to 45 MPa and stabilized. This pressure relief efficiency amounts to 79.5%. The blue lines represent changes in the peak ground acceleration (PGA) of the main roadway and pressure relief roadway. According to the PGA data, before pressure relief was implemented, the PGA of the main roadway remained within the range of 43-50 m/s$^2$, indicating significant pressure and a heightened risk of safety accidents. Following the pressure relief process, the PGA of the main roadway decreased rapidly, with a reduction rate of 81.2% within one day. This significant decline suggests a rapid shift in roadway stress, with the PGA of the main roadway stabilizing within the range of 8-12 m/s$^2$ postrelief. The stress and PGA changes observed in the pressure relief roadway are inverse to those in the main roadway, indicating that the stress was effectively transferred from the main roadway to the pressure relief roadway. Overall, the pressure relief cycle using this advanced pressure relief roadway method typically lasts approximately 5 days.

The microseismic events monitored during the pressure relief on December 14$^{th}$ are displayed in Figure 18. Figure 19 illustrates the proportion of microseismic events in the pressure relief roadway and main roadway, ranging from 0 to

(a) (b)

Figure 17: Installation position of system: (a) location of pressure relief roadway; (b) location of main roadway location.

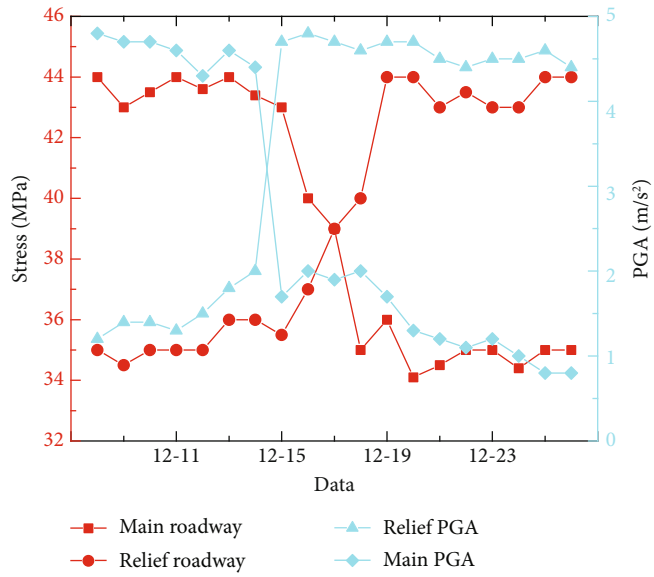


Figure 18: Monitoring data analysis.

50 m/s$^2$. Notably, 820 events occurred within the 40-50 m/s$^2$ range, accounting for the largest proportion of 41%. This suggests significant stress concentration in the pressure relief roadway. The proportion of microseismic events in the main roadway is within the 0~50 m/s$^2$ range. The largest proportion in this case is 36%, with 720 events occurring within the 10-20 m/s$^2$ range. These data indicate that the main roadway remains relatively stable with minimal vibrations

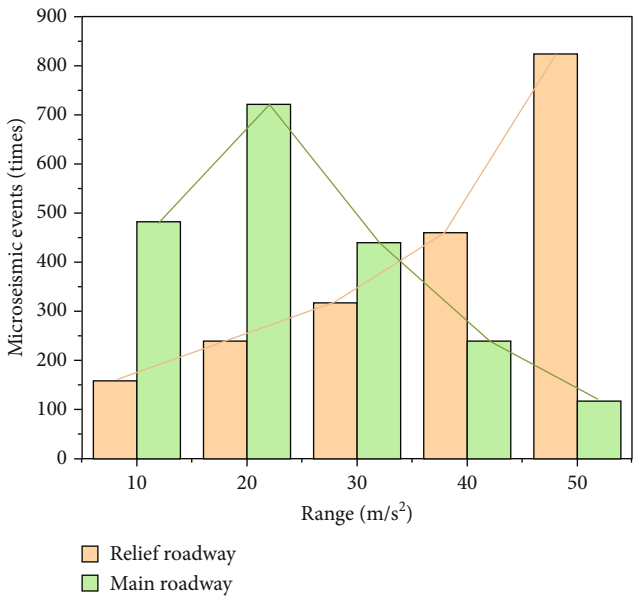


Figure 19: Distribution of microseismic events.

during the pressure relief process. Therefore, we infer that the pressure relief achieved using this method is effective.

## 7. Conclusions

(1) Based on a test conducted on the loose ring of the main roadway at the Sanshandao Gold Mine, it was observed that the loose ring has a range of 2.5 meters. The length of the on-site bolt was found to be 2 meters, which does not extend into the stable area. According to the bolt's drawing load test, when the bolt length exceeds 3 meters, it can withstand a drawing load of 250 kN, thereby meeting the safety support requirements. Consequently, the length of the roadway bolt support has been modified to 3 meters

(2) After conducting numerical simulations, it has been observed that the overall performance of scheme 1 surpasses that of scheme 2. Implementing scheme 1's pressure relief can effectively reduce the deformation of the main roadway by up to 20%. Although the pressure relief during advance mining in the tunnel may produce some effect, its impact is limited

(3) Through on-site measurements, it has been determined that the optimal pressure relief effect is achieved when the pressure relief roadway is situated 15 meters away from the main road. By implementing this pressure relief method, the maximum displacement of the roadway can be limited to within 100 mm. It is important to note that the stress is primarily concentrated within 0.2 meters of the pressure relief roadway, resulting in a pressure relief efficiency of approximately 80%

(4) The selection of pressure relief technology and methods for deep, high-stress tunnels is of utmost importance. By employing suitable pressure relief methods and support measures, it is possible to maintain the tunnel deformation within an acceptable range. Pressure relief in tunnels represents a significant technical approach, and the findings of this research can serve as a theoretical foundation for similar projects

## Data Availability

Data is available on request.

## Conflicts of Interest

The authors declare that they have no conflicts of interest.

## Acknowledgments

This work was supported by the National Key Research and Development Program (NKRDP) of China (2022YFC2904104), the National Natural Science Foundation of China (U23B2094), the Natural Science Foundation of Hunan Province, China (2024JJ6383), and the Outstanding Youth Project of Hunan Provincial Education Department (23B0444).

## References

[1] J. A. Hudson and J. P. Harrison, *Engineering Rock Mechanics: An Introduction to the Principles*, Elsevier, 2000.

[2] M. F. Cai, M. C. He, and D. Y. Liu, *Rock Mechanics and Engineering*, Science Press, 2002.

[3] Q. Lin, P. Cao, G. Wen, J. Meng, R. Cao, and Z. Zhao, "Crack coalescence in rock-like specimens with two dissimilar layers and pre-existing double parallel joints under uniaxial compression," *International Journal of Rock Mechanics and Mining Sciences*, vol. 139, article 104621, 2021.

[4] W. Wang, G. Cao, Y. Li et al., "Effects of freeze–thaw cycles on strength and wave velocity of lime-stabilized basalt fiber-reinforced loess," *Polymers*, vol. 14, no. 7, p. 1465, 2022.

[5] W. Wang, G. Cao, Y. Li et al., "Experimental study of dynamic characteristics of tailings with different reconsolidation degrees after liquefaction," *Frontiers in Earth Science*, vol. 10, article 876401, 2022.

[6] H. W. Wang, Y. D. Jiang, S. Xue et al., "Influence of fault slip on mining-induced pressure and optimization of roadway support design in fault-influenced zone," *Journal of Rock Mechanics and Geotechnical Engineering*, vol. 8, no. 5, pp. 660–671, 2016.

[7] J. Colint, C. N. Halldin, and J. Schall, "Best practices for dust control in coal mining," *Information Circular (National Institute for Occupational Safety and Health)*, vol. 9532, p. 119, 2021.

[8] Z. H. Xiu, W. Nie, J. Y. Yan et al., "Numerical simulation study on dust pollution characteristics and optimal dust control air flow rates during coal mine production," *Journal of Cleaner Production*, vol. 248, article 119197, 2020.

[9] X. Liu, H. Liu, C. Peng et al., "Distribution of in situ stress in northwest Jiaodong Peninsula," *Advances in Civil Engineering*, vol. 2022, Article ID 3934398, 10 pages, 2022.

[10] C. Peng, Y. Liu, M. D. Zhu et al., "Mechanical response and failure characteristics of granite under unloading conditions and its engineering application," *Periodica Polytechnica Civil Engineering*, vol. 67, no. 2, pp. 505–517, 2023.

[11] M. Esmaeili-Falak, H. Katebi, and A. Javadi, "Experimental study of the mechanical behavior of frozen soils-a case study of Tabriz subway," *Periodica Polytechnica Civil Engineering*, vol. 62, no. 1, pp. 117–125, 2015.

[12] E. F. Mahzad and K. Hooshang, "Stress analysis of segmental tunnel lining using artificial neural network," *Periodica Polytechnica Civil Engineering*, vol. 61, no. 4, pp. 664–676, 2015.

[13] M. W. Jiang, X. Wang, H. X. Liu, G. Li, X. Q. Liu, and C. L. Wang, "Optimization of drainage shaft wall is in complex geological environment," *Arabian Journal of Geosciences*, vol. 15, no. 1, p. 111, 2022.

[14] W. Yin, X. X. Miao, J. X. Zhang, and S. J. Zhong, "Mechanical analysis of effective pressure relief protection range of upper protective seam mining," *International Journal of Mining Science and Technology*, vol. 27, no. 3, pp. 537–543, 2017.

[15] X. Cheng, G. M. Zhao, Y. M. Li, X. R. Meng, and Q. Tu, "Key technologies and engineering practices for soft-rock protective seam mining," *International Journal of Mining Science and Technology*, vol. 30, no. 6, pp. 889–899, 2020.

[16] X. S. Liu, S. L. Song, Y. L. Tan et al., "Similar simulation study on the deformation and failure of surrounding rock of a large section chamber group under dynamic loading," *International Journal of Mining Science and Technology*, vol. 31, no. 3, pp. 495–505, 2021.

[17] S. C. Zhang, Y. Y. Li, B. T. Shen, X. Z. Sun, and L. Q. Gao, "Effective evaluation of pressure relief drilling for reducing rock bursts and its application in underground coal mines," *International Journal of Rock Mechanics and Mining Science*, vol. 114, pp. 7–16, 2019.

[18] G. Wu and L. Zhang, "Studying unloading failure characteristics of a rock mass using the disturbed state concept," *International Journal of Rock Mechanics and Mining Sciences*, vol. 41, p. 437, 2004.

[19] H. P. Xie, J. F. Liu, Y. Ju, and L. Z. Xie, "Fractal property of spatial distribution of acoustic emissions during the failure process of bedded rock salt," *International Journal of Rock Mechanics and Mining Sciences*, vol. 48, no. 8, pp. 1344–1351, 2011.

[20] H. Xie, L. Li, R. Peng, and Y. Ju, "Energy analysis and criteria for structural failure of rocks," *Journal of Rock Mechanics and Geotechnical Engineering*, vol. 1, no. 1, pp. 11–20, 2009.

[21] Z. K. Hou, H. L. Cheng, S. W. Sun, D. Q. Qi, and Z.-B. Liu, "Crack propagation and hydraulic fracturing in different lithologies," *Applied Geophysics*, vol. 16, no. 2, pp. 243–251, 2019.

[22] X. R. Liu, F. Xiong, D. S. Liu et al., "Theoretical study on relaxed surrounding rock pressure on shallow bias neighborhood tunnels under seismic load," *Periodica Polytechnica Civil Engineering*, vol. 65, p. 4, 2020.

[23] F. Dai, B. Li, N. Xu, and Y. Zhu, "Microseismic early warning of surrounding rock mass deformation in the underground powerhouse of the Houziyan hydropower station, China," *Tunnelling and Underground Space Technology*, vol. 62, pp. 64–74, 2017.

[24] S. Roateşi, "Analytical and numerical approach for tunnel face advance in a viscoplastic rock mass," *International Journal of Rock Mechanics and Mining Sciences*, vol. 70, pp. 123–132, 2014.

[25] M. Lei, D. Lin, W. Yang, C. Shi, L. Peng, and J. Huang, "Model test to investigate failure mechanism and loading characteristics of shal-low-bias tunnels with small clear distance," *Journal of Central South University*, vol. 23, no. 12, pp. 3312–3321, 2016.

[26] M. Mohtadinia, M. H. Ahmadi, M. M. Fasaghandis, B. H. Dibavar, and S. M. Davarpanah, "Statistical and numerical study of chipping and cracking in segmental lining," *Periodica Polytechnica Civil Engineering*, vol. 64, no. 3, pp. 869–886, 2020.

[27] M. F. Xu, S. C. Wu, Y. T. Gao, J. Ma, and Q. L. Wu, "Analytical elastic stress solution and plastic zone estimation for a pressure-relief circular tunnel using complex variable methods," *Tunnelling and Underground Space Technology*, vol. 84, pp. 381–398, 2019.

[28] B. B. Chen and C. Y. Liu, "Optimization and practice for partition pressure relief of deep mining roadway using empty-hole and deep-hole blasting to weaken coal," *Geofluids*, vol. 2021, Article ID 9335523, 16 pages, 2021.

[29] Y. Luo, K. Xu, J. Huang et al., "Impact analysis of pressure-relief blasting on roadway stability in a deep mining area under high stress," *Tunnelling and Underground Space Technology*, vol. 110, article 103781, 2021.

[30] W. Geng, W. Wang, G. Huang et al., "Case study on the secondary support time and optimization of combined support for a roadway under high in-situ stress," *Geomechanics and Geophysics for Geo-Energy and Geo-Resources*, vol. 10, no. 1, p. 66, 2024.